

Effect of Tomography Resolution on Calculation of Microstructural Properties for Lithium Ion Porous Electrodes

J. Le Houx^a, M. Osenberg^{b,c}, M. Neumann^d, J. Binder^e, V. Schmidt^d, I. Manke^c,
T. Carraro^{cf} and D. Kramer^a

^a Energy Technology Research Group, Faculty of Engineering and Physical Sciences,
University of Southampton, SO17 1BJ, United Kingdom

^b Institut für Werkstoffwissenschaften und -technologien, Technische Universität Berlin,
10623 Berlin, Germany

^c Institute of Applied Materials, Helmholtz-Zentrum Berlin für Materialien und Energie
(HZB), 14109 Berlin, Germany

^d Institute of Stochastics, Ulm University, 89069 Ulm, Germany

^e Institute for Applied Materials, Karlsruhe Institute of Technology, 76344 Eggenstein-
Leopoldshafen, Germany

^{cf} Faculty of Mechanical Engineering, Applied Mathematics, Helmut Schmidt University
/ University of the Federal Armed Forces Hamburg, 22043 Hamburg, Germany

This work uses an open-source, data-driven, image-based modelling framework; OpenImpala. Lithium Iron Phosphate (LFP) electrode samples were imaged using micro-CT. Two scans were performed using the Zeiss 160 kVp Versa 510 at the University of Southampton. The two scans were both carried out on the same sample and using the same focal point, this is so they could be used as a direct comparison to see how porosity and tortuosity changed with spatial resolution. It is found that the Bruggeman correlation significantly underestimates the tortuosity compared to the OpenImpala calculated results. It is also found that there is a larger statistical variability in the 801 nm results, whereas the 400 nm results have a much smaller standard deviation. These results were compared to computer-generated images based on FIB/SEM tomographic data of a single Nickel Manganese Cobalt Oxide (NMC) porous active particle and found to have the same trends.

Motivation and Significance

Mathematical models have been used to simulate the physical and electrochemical processes occurring inside batteries in order to aid understanding and design. Newman et al. developed one of the most popular lithium ion battery models based on the porous electrode and concentrated solution theory. Newman's pseudo-2D (P2D) model assumes that the porous electrode is made of equally sized, isotropic, homogeneous spherical particles. It has been shown that battery electrodes are actually very heterogeneous structures [1] and therefore more complex approaches are required in order to fully characterise the transport processes occurring within the battery.

Recent advances in imaging technology have made the characterisation technique widely available across both industry and academia [2]. Three-dimensional material

microstructures can now be used to calculate effective homogenised material properties [3] [4] or be used directly as the computational domain to solve relevant physical equations [5] [6]. These processes are known as image-based modelling.

Furthermore, [7] has reviewed the open literature in physics-based lithium ion porous electrode modelling. Physically based models, coupled with experimental validation, have helped reveal greater scientific understanding of the processes inside the battery. The porous electrode is of specific interest as it is where lithium de/intercalation occurs. It is found that there has been a general trend to improve the accuracy of physically based models by including the heterogeneity of the porous electrode structure. This contrasts with the traditional method of assuming the electrode to be a homogeneous structure through using the Bruggeman relation, where only the volume fraction of the transport phase is considered. In the present paper, tomographic image data has been used to include this complexity by numerical transport modelling. For further results concerning the influence of geometrical microstructure characteristics on effective transport going beyond the Bruggeman relation, the reader is referred to [8-11].

One of the remaining challenges in the field, outlined in [7], is to fully characterize the effects that image resolution has on transport properties, such as porosity and tortuosity. First investigations regarding the effect of image resolution on the results of simulation can be found in [6], however, more rigorous study is required to fully characterise the effects. Imaging the same electrode sample at a number of resolutions, at the same point in space and with the same overall dimensions, would allow a direct comparison of the effect of resolution on structural properties key to solving transport equations, such as tortuosity and porosity. This study sets out to improve this understanding.

While scanning electron microscopy (SEM) and transmission electron microscopy (TEM) have both been used extensively in electrode analysis, the scattered electrons mean that SEMs cannot capture 3-dimensional data sets as they do not penetrate the target [12] and are therefore unsuitable for this purpose. TEMs transmit electrons through the sample before being detected, offering a way of capturing the internal detail such as crystal structure and morphology [13]. Additionally, TEMs can achieve much smaller resolutions by an order of magnitude, with some reports of 50 pm. However, when considering the thickness of a standard lithium ion electrode, 50 μm , TEM cannot penetrate deep enough to capture all the microstructure [14], therefore, it is also unsuitable.

Two popular techniques that do offer suitable 3-dimensional quantification of porous materials at sub-micron-scale resolution are focused ion beam-scanning electron microscopy (FIB-SEM) and micro-scale X-ray computed tomography (micro-CT). Both FIB-SEM and micro-CT have been shown to be suitable for capturing fine structures of porous components, many examples can be found in fuel cell research [15-18] as well as battery research [2][19][20]. FIB-SEM combines the imaging capabilities of SEM with the milling and cross-sectioning abilities of FIB. This enables serial-sectioning of a target sample, producing high-resolution 3D constructions. Micro-CT systems use a conventional X-ray CT system, with the addition of finer focusing components which allows the 3D microstructure of the material to be captured at sub-micron-scale. FIB-SEM, however, is a destructive imaging technique as it mills the target away uses a controlled beam of positively charged gallium particles [21]. This means that in-situ

testing or re-testing of a battery would not be possible using this method. State of the art CT systems can achieve resolutions of 50 nm, meaning sufficient microstructural detail can be captured. Additionally, [2] shows that a pixel size in the order of 100 nm provides consistent measurements for porosity and tortuosity calculations.

Finite element-based models have been used extensively to simulate lithium-ion batteries [5] however they have been shown to be computationally expensive to mesh the image data. Finite difference/volume schemes use a regularly discretised mesh and are usually quicker to implement, as the voxel dataset can be used directly, but they can result in approximation errors. This work uses an open-source, data-driven, image-based modelling framework, OpenImpala, that is capable of modelling transport processes in lithium-ion battery electrodes. OpenImpala uses a finite volume scheme to solve transport equations directly on the as imaged microstructure, solving for effective diffusion, tortuosity and porosity [22].

Electrode microstructural image data is obtained experimentally using micro-CT at two resolutions. Image data is also generated computationally using level set functions based on tomographic data. These datasets are then used to compare geometric parameters as calculated by OpenImpala.

X-Ray Tomography of Lithium Iron Phosphate Electrodes

Experimental Setup

Lithium iron phosphate (LFP) is used extensively as a battery anode material, finding commercial use in a number of applications such as electric vehicles, utility scale stationary energy storage applications and backup power. At the University of Southampton there is capability to manufacture both coin and pouch cells using this material. The material is mixed into a slurry with a conductive binder and then coated onto an aluminium current collector using a doctor blade. The electrode is then calendered, a process where a series of hard pressure rollers are used to smooth the sheet of electrode material across the current collector. The electrode is approximately 40 μm in thickness, therefore if the sample was directly mounted onto the aluminium rod a large amount of beam scattering would be present from the aluminium. Instead the electrode was rolled into a tube and then mounted on top of the aluminium rod, held in place by epoxy. This allowed the scintillator and beam source distance to be reduced to the diameter of the mounting rod, and also moved the focal point away from the highly scattering aluminium, improving image quality.

Two scans were performed using the Zeiss 160 kVp Versa 510 at the University of Southampton. The first with a 15 s exposure time and 2401 projections across an image angle of 180° , using a 20x optical magnification to capture a voxel size of 801 nm. The second with a 50 s exposure and 3201 projections, using a 40x optical magnification to capture a voxel size of 400 nm. Both used a voltage of 80 kV and a power of 6 W, the power was slightly higher than usual in order to better resolve the image. The two scans were both carried out on the same sample and using the same focal point, this is so they could be used as a direct comparison to see how porosity and tortuosity values changed with spatial resolution.

Results

The results of the scans can be seen in Figure 1. In particular, Figure 1 (a) shows an overall scan of the electrode from the top view at a much larger resolution, this image is then used to find a region of interest to perform subsequent scans. Figure 1 (b) shows a single tomographic slice from the 801 nm scan, the LFP electrode can be seen coated onto the aluminium current collector, this scan was used to select a sub-volume for further analysis. This equivalent sub-volume for both resolution scans was then used to directly compare the impact of scan resolution on the properties obtained. Figures 1 (c) and (d) show the raw image data at 801 nm and 400 nm voxel size respectively. This raw image data is then post-processed through using an anisotropic diffusion filter and the greyscale data is equalised across the histogram to produce more refined peaks and troughs. The results of this post-processing are shown in Figures 1 (e) and (f). Finally, this data is segmented into two phases, solid and liquid, using a simple interactive thresholding to produce Figures 1 (g) and (h). This post-processing was carried out using the commercial software package, Avizo. Comparing these two figures visually it is possible to see a difference in the detail of the images. Large pores and regions of solid are still present in the 801 nm scan, however, a significant amount of detail has been lost by using a lower resolution. In order to quantify this, six sub-volumes were taken from both resolutions and these twelve datasets were used to calculate porosity and tortuosity. The tortuosity is calculated as follows in each direction for each sub-volume dataset:

$$D^{\text{eff}} = D \frac{\varepsilon}{\tau} \quad (1)$$

Where ε is the volume fraction of the conducting phase, D is the intrinsic diffusivity of the conducting phase and D^{eff} is the effective diffusivity through the porous volume where the second phase is insulating [23][24]. A value for the tortuosity is also calculated through using the Bruggeman relationship, defined as:

$$\tau = \varepsilon^{1-\alpha} \quad (2)$$

where τ is the tortuosity, ε is the porosity and α is the Bruggeman exponent, usually assumed to be 1.5 [25]. In order to compare these values, direction-averaged values of tortuosity are obtained for each data sub-volume, the results of these can be seen in Figure 2. It can be seen that the Bruggeman relationship significantly underestimates the tortuosity in comparison to CT obtained values, which is consistent with the literature. It is also noted that the 400 nm scan corresponds to a smaller value for the tortuosity in comparison to the other CT obtained values, which is again in agreement with the literature [2]. Shearing et al. state that 'the improvements in scan resolution reveal smaller pore geometries that contribute to higher porosity, improved connectivity and a corresponding lower tortuosity'. Finally, it is noted that there is a larger variance in values across the six datasets for the 801 nm resolution when compared to the 400 nm. This might be due to the scan resolutions inability to resolve all features, leading to more varied results across the six datasets. Full data for these calculations is given in Table 1.

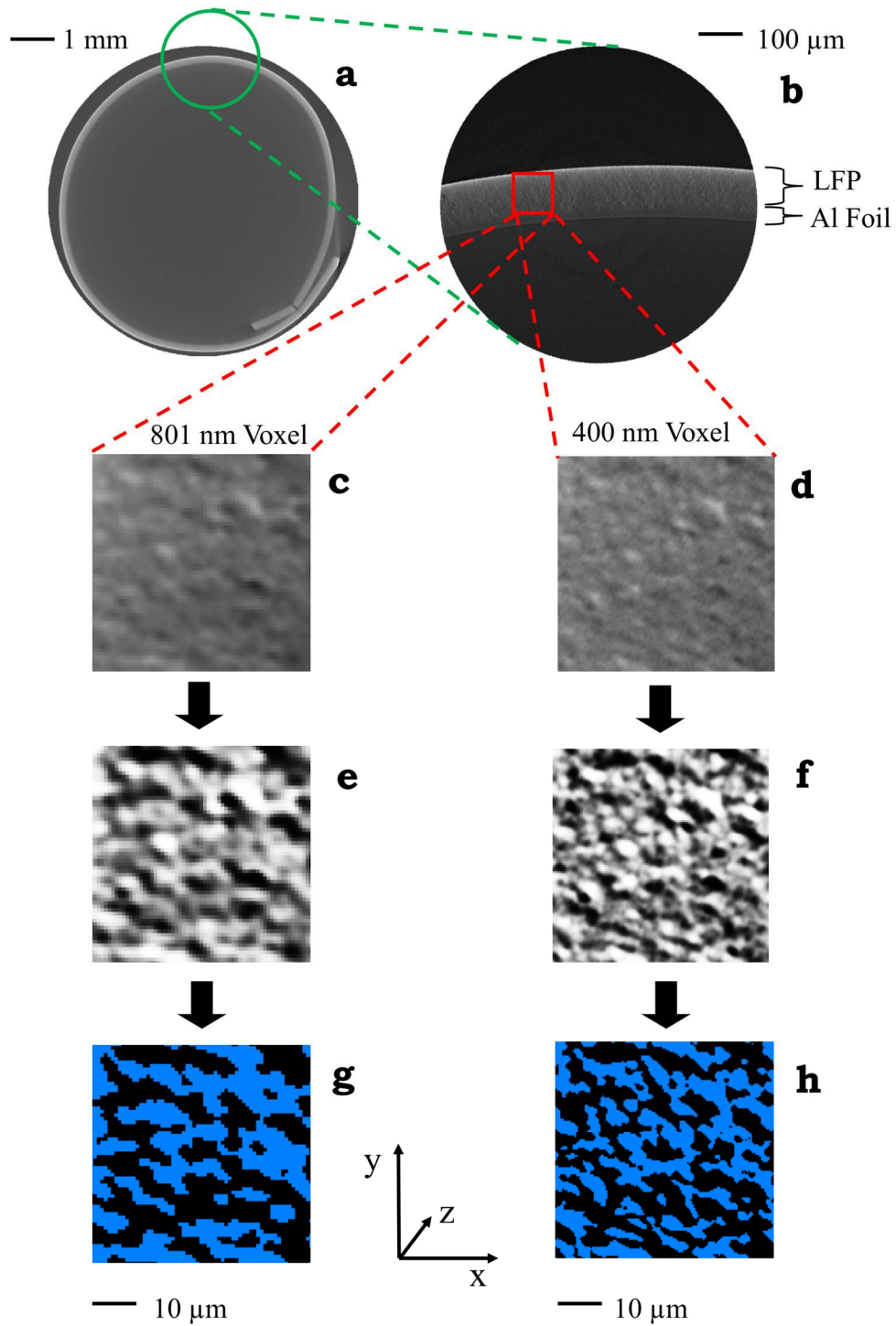


Figure 1. X-ray tomography of an LFP electrode detailing (a) the mounting, (b) the region of interest; 801 nm voxel scans of (c) raw data, (e) equalised and filtered data, and (g) 2-phase thresholded data; and 400 nm voxel scans of (d) raw data, (f) equalised and filtered data, and (h) 2-phase thresholded data.

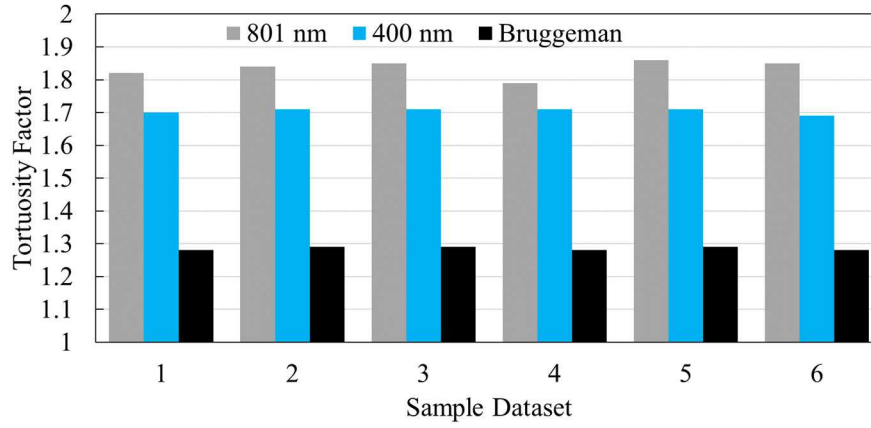


Figure 2. Variability of tortuosity calculated for two resolution scans, 400 nm and 801 nm, and through using the Bruggeman relationship across six data samples.

TABLE I. Tortuosity calculated for six sub-volumes from two-resolution X-ray tomography scans of an LFP electrode

Voxel Volume	63 x 63 x 63						Voxel Size			801 nm
Sample Set	1			2			3			
Direction	x	y	z	x	y	z	x	y	z	
D^{eff}	0.289	0.351	0.353	0.296	0.346	0.329	0.285	0.353	0.314	
Tortuosity	2.07	1.70	1.69	2.00	1.71	1.80	2.05	1.65	1.86	
Direction Averaged Tortuosity	1.82			1.84			1.85			
Phase Volume	59.6%			59.2%			58.4%			
Bruggeman	1.30			1.30			1.31			
Sample Set	4			5			6			
Direction	x	y	z	x	y	z	x	y	z	
D^{eff}	0.291	0.374	0.339	0.280	0.349	0.332	0.283	0.340	0.340	
Tortuosity	2.04	1.59	1.75	2.10	1.69	1.78	2.08	1.73	1.73	
Direction Averaged Tortuosity	1.79			1.86			1.85			
Phase Volume	59.3%			59.0%			58.9%			
Bruggeman	1.30			1.30			1.30			

Voxel Volume	125 x 126 x 126						Voxel Size			400 nm
Sample Set	1			2			3			
Direction	x	y	z	x	y	z	x	y	z	
D^{eff}	0.333	0.384	0.365	0.323	0.405	0.344	0.315	0.403	0.346	
Tortuosity	1.83	1.59	1.67	1.87	1.49	1.76	1.91	1.49	1.74	
Direction Averaged Tortuosity	1.70			1.71			1.71			
Phase Volume	60.9%			60.4%			60.2%			
Bruggeman	1.28			1.29			1.29			
Sample Set	4			5			6			
Direction	x	y	z	x	y	z	x	y	z	
D^{eff}	0.314	0.405	0.357	0.318	0.402	0.347	0.336	0.384	0.362	
Tortuosity	1.93	1.50	1.70	1.89	1.50	1.74	1.81	1.59	1.68	
Direction Averaged Tortuosity	1.71			1.71			1.69			
Phase Volume	60.7%			60.3%			60.9%			
Bruggeman	1.28			1.29			1.28			

For the samples investigated the tortuosity was found to vary in all three directions. It is especially noted that for the 400 nm scans, the tortuosity in the y -direction is consistently at a lower value (an average of 1.52 compared to 1.87 and 1.72 in the x - and z -direction respectively). It is conceivable that this result may be due to the processing steps used to manufacture the electrode, e.g. calendaring where the pores in the x - and z -directions would be reduced in size, however further investigation is required to confirm this hypothesis.

FIB/SEM Tomography of a Lithium Nickel Manganese Cobalt Oxide Structured Particle

Experimental Setup

Like LFP, Lithium Nickel Manganese Cobalt Oxide (NMC) is also a very common composition used in many applications. NMC based batteries are, for example, widely used in the auto motive industry, power tools or e-bikes. To achieve high power densities it is important that the electrolyte can reach as much active material as possible. Therefore, a high material surface is desirable. The material shown in Figure 3 was produced with high power applications in mind at Karlsruher Institute of Technology and consequently is highly hierarchically structured. The active material was first grinded from pristine $\text{Li}(\text{Ni}_{1/3}\text{Mn}_{1/3}\text{Co}_{1/3})\text{O}_2$ powder (NM-3100, Toda America), next it was spray dried and finally calcined at 850°C .

The FIB/SEM tomography was performed at Helmholtz-Zentrum Berlin using a Zeiss Crossbeam 340 equipped with a Gemini I VP column. For the serial section milling the ion gun was operated at 30 kV with a gallium ion current of 300 pA. After each milling step a SEM image was captured under an angle of 54° . The electron gun was operated at 2 kV. The pixel size was synchronized to the milling depth resulting in an isotropic voxel size of 10 nm.

3D data segmentation and reconstruction. The raw volume data was drift corrected by utilizing image features that were not part of the milled surface. As these features have not been destroyed during the milling process they were suitable for drift correction and could be tracked and stabilized. After stabilization the dataset was cropped removing all parts that have not been ion milled such as the preprocessed outer areas. For intensity normalization the data set was duplicated and a minimum filter with a filter radius larger than the primary particles was applied. The filtered data set was further blurred, resulting in a gradient mask reflecting the intensity fading of the milled surface area in the original data set. After subtracting the intensity mask from the original data set a Niblack local threshold was applied resulting in the final binary reconstruction. All reconstruction steps have been performed using the freeware Fiji. The reconstructed final volume size measured $20 \times 20 \times 20 \mu\text{m}^3$.

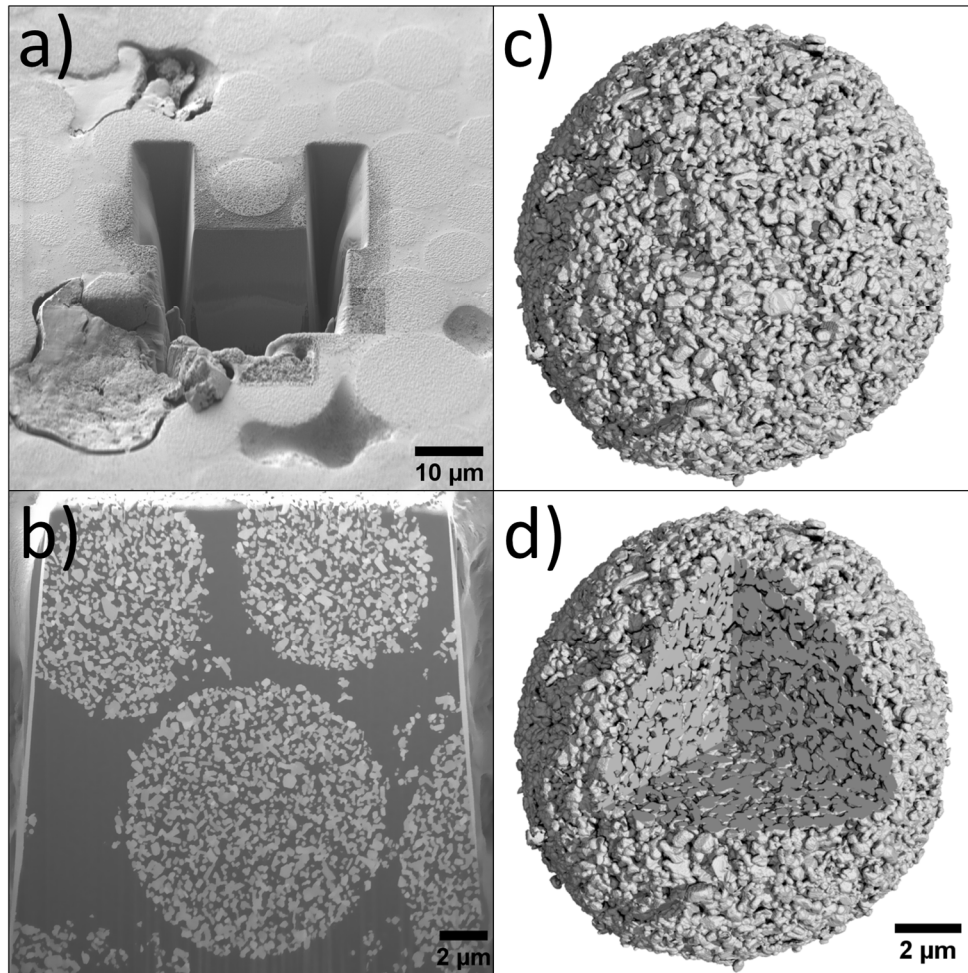


Figure 3. FIB/SEM tomography performed on a NMC cathode particle showing (a) the preprocessed area on the sample before the serial section tomography is performed, (b) one slice of the serial section during the measuring process, (c) a 3D render of one of the tomographed NMC cathode particles and (d) the same particle but with one section virtually removed to reveal its inner structure.

Figure 3 shows a FIB/SEM tomographic analysis of a single NMC cathode battery particle. FIB/SEM tomography allows to cut slicewise through a whole particle with a spatial resolution of a few nanometers. Figure 3 (a) shows an overview on the NMC electrode location where a single NMC particle was chosen. Figure 3 (b) shows a cut through several particles. From the particle in the centre a complete 3D data set was created (Figures 3 (c) and (d)). It contains all structural and morphological information of the NMR particle with a spatial resolution of roughly 10 nm.

NMC particle sizes are typically between a few μm and 30 μm . For this study particles of typical sizes around 4-8 μm have been chosen. These particles consist of much smaller primary particles with sizes around 20-150 nm (see Figure 3). Therefore, a measurement technique like FIB/SEM tomography with a spatial resolution of about 10 nm is ideally suited to create 3D data sets that contain all the necessary information for realistic simulation studies.

Results

After binarization of image data, a voxel representation of the pore phase and the material phase is obtained. To perform the numerical study shown here, the geometry of the porous microstructure of the single NMC particle has been represented by several thousand level set functions. For the tortuosity computation, the material phase has been represented by a union of voxelised particles using the watershed algorithm described in [26]. Then, each voxelised particle undergoes a smoothing process, where it is analytically described by so-called spherical harmonics functions [27]. The analytical representation of the pore phase is then given by the complement of the union of particles. The idea is to define a model of the geometry, based on tomographic data, that can be used to compute the tortuosity with different resolutions. Two datasets have been produced from the same microstructure, using two resolutions: a 499 cubic voxel set and a 998 cubic voxel set.

Concentration plots of the 499 cubic voxel set in the x, y and z directions are shown in Figure 1. OpenImpala is an easily parallelisable code written specifically for high performance computing, allowing large image datasets to be used to compute effective transport parameters. The simulations were run on the University of Southampton's HPC system, Iridis 5. This consists of 464 compute nodes, of 40 cores per node, running dual 2.0 GHz Intel Skylake processors with 192 Gb of DDR4 memory. The calculations for the 499 voxel set that would have previously taken hours and days to solve, can now be solved in around 2 minutes with suitable computing architecture using OpenImpala. Furthermore, large scale datasets typical of modern tomography, 10^9 voxels, can be analysed to obtain highly precise transport coefficients.

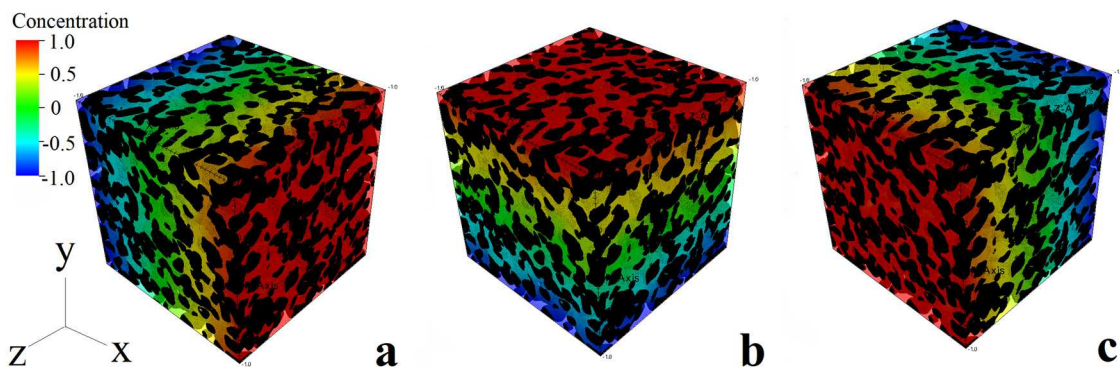


Figure 4. Concentration plots of 499 voxel cubic dataset for (a) x-, (b) y-, and (c) z-directions

The results of the calculations can be seen in Table 2. The pore phase and material phase of both resolution datasets were analysed in each direction. In the material phase, similar values for direction averaged tortuosity and phase volume are calculated to the experimentally obtained image datasets. Additionally, the same trend of decreasing tortuosity with improved resolution is noted. Since both data sets were obtained by the same level set model, the same phase volumes for the two resolutions was expected.

TABLE 2. Tortuosity calculated for both pore and material phases based on two resolutions of a single active NMC particle

Voxel Volume	Pore Phase						Material Phase					
	499 x 499 x 499			998 x 998 x 998			499 x 499 x 499			998 x 998 x 998		
Direction	x	y	z	x	y	z	x	y	z	x	y	z
D^{eff}	0.179	0.200	0.194	0.188	0.214	0.210	0.333	0.335	0.343	0.348	0.344	0.361
Tortuosity	2.12	1.90	1.96	2.02	1.77	1.81	1.86	1.85	1.85	1.78	1.80	1.72
Direction Averaged Tortuosity	2.00			1.87			1.86			1.77		
Phase Volume	38.0%			38.0%			62.0%			62.0%		
Bruggeman	1.62			1.62			1.27			1.27		

Conclusions

In this work the effective transport coefficients of a porous LFP electrode and of a porous single NMC active particle have been computed using tomographic data. The computed tortuosity has been compared to the Bruggeman formula. It is found that the Bruggeman correlation significantly underestimates the tortuosity compared to the OpenImpala calculated results for both case studies. Furthermore, a comparison of resolution study was carried out to see how this affects results obtained.

Regarding the LFP electrode, it is found that there is a larger statistical variability in the data with finer resolution (801 nm), whereas the coarser resolution (400 nm) results have a much smaller standard deviation. In both case studies, a finer resolution leads to a reduction of the tortuosity.

This work has made use of a single-physics, image-driven computational model, OpenImpala. Further work will be done to study more precisely the effect of the image resolution to the computed effective coefficients. The 998 voxel data set of the single particle has been also used to show the capability of the implementation to deal with huge data sets. In future works, this code can be used to analyse larger electrode reference volume elements. This will allow to study the microstructure heterogeneity of porous electrodes with a precision not yet shown.

Acknowledgments

This work was financially supported by the EPSRC Centre for Doctoral Training (CDT) in Energy Storage and its Applications [grant ref: EP/R021295/1]. The authors acknowledge the μ -VIS X-ray Imaging Centre at the University of Southampton for provision of tomographic imaging facilities, supported by EPSRC grant EP-H01506X. The authors acknowledge the use of the IRIDIS High Performance Computing Facility, and associated support services at the University of Southampton, in the completion of this work. MO, MN, VS, IM, JB, TC acknowledge financial funding by the German Federal Ministry for Economic Affairs and Energy (BMWi) granted through Project Management Jülich (03ET6095A, 03ET6095B, 03ET6095C, 03ET6095E).

References

1. Tjaden, B., Cooper, S.J., Brett, D.J., Kramer, D. and Shearing, P.R., in *Curr. Opin. Chem. Eng.*, **12**, p.44-51 (2016).
2. Ojha, M., Le Houx, J., Mukkabla, R., Kramer, D., Wills, R.G.A. and Deepa, M., in *Electrochim. Acta*, **309**, p.253-263 (2019).
3. Gully, A., Liu, H., Srinivasan, S., Sethurajan, A.K., Schougaard, S. and Protas, B., in *J. Electrochem. Soc.*, **161**(8), p.E3066-E3077 (2014).
4. Richardson, G., Denuault, G. and Please, C.P., in *J. Eng. Math.*, **72**(1), p.41-72 (2012).
5. Kashkooli, A.G., Farhad, S., Lee, D.U., Feng, K., Litster, S., Babu, S.K., Zhu, L. and Chen, Z., in *J. Power Sources*, **307**, p.496-509 (2016).
6. Shearing, P.R., Brandon, N.P., Gelb, J., Bradley, R., Withers, P.J., Marquis, A.J., Cooper, S. and Harris, S.J., in *J. Electrochem. Soc.*, **159**(7), p.A1023-A1027 (2012).
7. Le Houx, J. and Kramer, D. in *Energy Rep.*, **Forthcoming**, (2020).
8. Torquato, S. in *Random Heterogeneous Materials: Microstructure and Microscopic Properties*, Springer (2002).
9. Jeulin, D., in *CR Mecanique*, **340**, p. 219-229 (2012).
10. Gaiselmann, G., Neumann, M., Pecho, O., Hocker, T., Schmidt V., and Holzer, L., in *AIChEJ*, **60**, p.1983-1999 (2014).
11. Neumann, M., Stenzel, O., Willot, F., Holzer, L., and Schmidt, V., in *Int. J. Solids Struct.*, **184**, p. 211-220 (2020).
12. Goldstein, J.I., Newbury, D.E., Michael, J.R., Ritchie, N.W., Scott, J.H.J. and Joy, D.C., in *Scanning Electron Microscopy and X-ray Microanalysis*, Springer (2017).
13. Grothausmann, R., Zehl, G., Manke, I., Fiechter, S., Bogdanoff, P., Dorbandt, I., Kupsch, A., Lange, A., Hentschel, M., Schumacher, G. and Banhart, J., in *Int. J. Mater. Res.*, **103**, p. 135-136 (2012).
14. Williams, D.B. and Carter, C.B., in *The Transmission Electron Microscope.*, p. 3-17, Springer (1996).
15. Ostadi, H., Rama, P., Liu, Y., Chen, R., Zhang, X.X. and Jiang, K., in *J. Membr. Sci.*, **351**(1-2), p.69-74 (2010).
16. Ziegler, C., Thiele, S. and Zengerle, R., in *J. Power Sources*, **196**(4), p.2094-2097 (2011).
17. Zils, S., Timpel, M., Arlt, T., Wolz, A., Manke, I. and Roth, C., in *Fuel Cells*, **10**(6), p. 966-972 (2010).
18. Gaiselmann, G., Tötzke, C., Manke, I., Lehnert, W. and Schmidt, V., in *J. Power Sources*, **257**, p.52-64 (2014).
19. Arlt, T., Schröder, D., Krewer, U. and Manke, I., in *Phys. Chem. Chem. Phys.*, **16**(40), p.22273-22280 (2014).
20. Moroni, R., Börner, M., Zielke, L., Schroeder, M., Nowak, S., Winter, M., Manke, I., Zengerle, R. and Thiele, S., in *Sci. Rep.*, **6**, p.30109 (2016).
21. Wargo, E.A., Kotaka, T., Tabuchi, Y. and Kumbur, E.C., in *J. Power Sources*, **241**, p.608-618 (2013).
22. Le Houx, J., and Kramer, D., in *ECS Meet. Abstr.*, MA2020-01, **539**(2020).
23. Cooper, S.J., Bertei, A., Shearing, P.R., Kilner, J.A. and Brandon, N.P., in *SoftwareX*, **5**, p.203-210 (2016).
24. Wiener, O., in *Abhdlgn. d. sächs. Ges. d. Wiss.(math.-phys. Kl.)*, **32**, p.507-604 (1912).

25. Shearing, P.R., Howard, L.E., Jørgensen, P.S., Brandon, N.P. and Harris, S.J., in *Electrochem. Commun.*, **12**(3), p.374-377 (2010).
26. Spettl, A., Wimmer, R., Werz, T., Heinze, M., Odenbach, S., Krill III, C.E., and Schmidt, V., in *Model. Simul. Mater. Sci. Eng.*, **23**, 065001 (2015).
27. Feinauer, J., Spettl, A., Manke, I., Strege, S., Kwade, A., Pott, A. and Schmidt, V., in *Mater. Charact.*, **106**, p. 123-133 (2015)